Supporting Information

Two-photon brightness of azobenzene photoswitches designed for glutamate receptor optogenetics

Elizabeth C. Carroll[a], Shai Berlin[a], Joshua Levitz[a], Michael A. Kienzler[a], Zhe Yuan[a], Dorte Madsen[b], Delmar S. Larsen[a], and Ehud Y. Isacoff[a,c,d,1]

Supporting Methods

Tissue culture and transfection. Dissociated postnatal hippocampal neurons (P0-P5) were prepared from Sprague Dawley rats (Charles River) at high density (80K cells/coverslip) and transfected using the Calcium-Phosphate transfection method as described previously (1), with 1 µg of cDNA encoding LA-LiGluR (GluK2-L439C-K456A) and 0.3 µg of EGFP. The additional point mutation (K456A) reduces glutamate affinity and quickens receptor recovery to glutamate desensitization (2). HeLa cells were maintained in DMEM with 5% FBS and transiently transfected with (in µg): 0.8-1 CMV-LiGluR6 and 1 CMV-R-GECO1.0 (red-calcium indicator (3)), using Lipofectamine 2000 (Invitrogen). Functional imaging was performed 2-3 days after transfection. Prior to imaging, cells were labeled with 100 µM L-MAG0$_{460}$ and treated with 0.3 mg/mL concavalin A (Sigma) to block desensitization of LiGluR. HEK293 and 293T cells were maintained in DMEM with 5% FBS and transiently transfected 24-36 hrs prior to experiments with (in µg): 0.7 LimGluR2 (mGluR2-L300C) or LimGluR3 (mGluR3-Q306C), 0.7 GIRK1-F137S and 0.1 tdTomato using Lipofectamine 2000. All cells were grown at 37°C.

Electrophysiology. Patch clamp recordings used a Multipatch 700B amplifier in the whole cell mode. Recordings were carried out after 15 DIV for hippocampal neurons. For LiGluR experiments, cells were incubated with 100 µM of either L-MAG0 or L-MAG0$_{460}$ for 45 min at 37°C, 5% CO_2. The labeling solution contained (in mM): 150 NMDG-HCl, 3 KCl, 0.5 $CaCl_2$, 5 $MgCl_2$, 10 HEPES, 5 D- glucose, pH 7.4. Cells were voltage-clamped at -60 mV. Pipettes had resistances of 8-12 MΩ and were filled with a solution containing (in mM): 140 K-gluconate, 10 NaCl, 2 MgATP, 1 $CaCl_2$, 2 $MgCl_2$ 10 HEPES, 5 EGTA, pH 7.4. The extracellular recording solution contained (in mM): 138 NaCl, 1.5 KCl, 1.2 $MgCl_2$, 10 D-glucose, 2.5 $CaCl_2$, 10 HEPES, pH 7.3. For LimGluR experiments HEK293 or 293T cells were incubated in 50 µM D-MAG-0$_{460}$ for 45-60 minutes at room temperature in a labeling solution containing (in mM): 135 NaCl, 5.4 KCl, 10 Hepes, 2.5 $CaCl_2$, 1 $MgCl_2$, pH 7.4. Extracellular high potassium recording solution contained (in mM): 120 KCl, 25 NaCl, 10 Hepes, 2 $CaCl_2$, 1 $MgCl_2$, pH 7.4. Pipettes had resistances of 6-10 MΩ and were filled with a solution containing (in mM): 140 KCl, 10 HEPES, 3 Na_2ATP, 0.2 Na_2GTP, 5 EGTA 3 $MgCl_2$, pH 7.4. Cells were voltage clamped at -60 mV. Electrophysiological recordings were digitized using Matlab (Mathworks), which was also used to synchronize illumination by means of analog signals controlling

either an LED driver (Thorlabs), or Pockel's cell (ConOptics). The 470 nm LED focal spot size was measured by knife edge to have a Gaussian xy-profile with $1/e^2$ diameter 200 ± 10 µm.

General synthetic methods. Unless otherwise noted: all reactions were monitored with Merck silica gel 60 F_{254} plates and visualized with 254 nm light, iodine on silica, or a charring solution of ceric ammonium molybdate (CAM). Flash chromatography was carried out using Agela Technologies 32-63 D 60 Å silica gel (normal phase) or 50 µm FLASH C18 silica gel (reverse phase). All chemicals were used as obtained from commercial sources. Non-aqueous reactions were carried out under nitrogen atmosphere and magnetically stirred in oven-dried glassware. Unless dry-loading the flash column, all organic extracts were washed with brine, dried over sodium sulfate and filtered through filter paper; solvents were then removed with a rotary evaporator at aspirator pressure. All NMR spectra were measured in deuterated chloroform ($CDCl_3$) or methanol (CD_3OD) with Bruker AV, AM, or DRX spectrometers at 400 MHz, 500 MHz, and 600 MHz for ^1H spectra and 151 MHz for ^{13}C spectra. Spectra were calibrated to residual solvent peaks as reported by Gottlieb and Nudelman (4) and processed using MestReNova v. 7.0 software. Optical rotations were measured using a Perkin-Elmer 241 Polarimeter at 25 °C and 589 nm, sample concentrations are reported in g/100 ml. High resolution mass spectra (HRMS) were obtained using the Micro-Mass Facility operated by the College of Chemistry, University of California at Berkeley using electrospray ionization (ESI).

Scheme S1. Synthetic route used for D-MAG0$_{460}$.

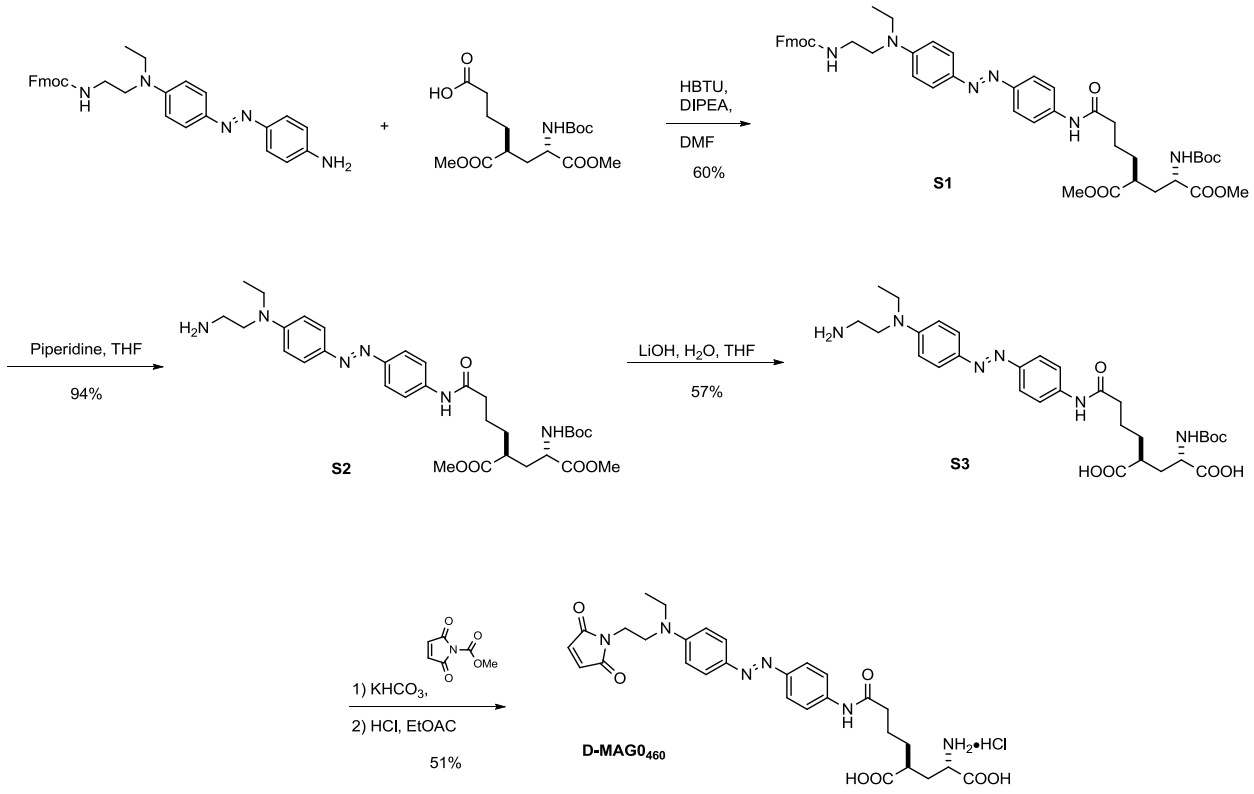

Synthetic procedures

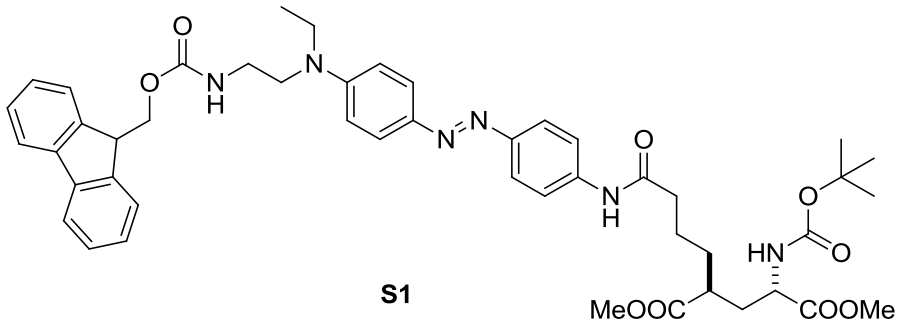

S1

Azobenzene S1. Previously described glutamate derivative (5) (251 mg, 0.692 mmol) was dried by reconcentration from benzene and placed under high vacuum for 1 h. It was then combined in a flask with azobenzene (6) (368 mg, 0.725 mmol), DIPEA (0.45 mL, 2.75 mmol), HBTU (275 mg, 0.725 mmol), and dissolved in DMF (20 mL). After stirring for 3 days, the reaction was diluted with EtOAc and then extracted 3 times with brine; the organic phase was dried and concentrated. Column chromatography on silica gel (dry load, 50% EtOAc in CH_2Cl_2) gave 355 mg (60%) of azobenzene **S1** as a red solid.

R_f 0.36 (20% EtOAc in CH_2Cl_2); ^{1}H NMR (600 MHz, MeOD) δ 7.72 (m, 6H), 7.64 (d, *J* = 7.6 Hz, 2H), 7.50 (d, *J* = 7.4 Hz, 2H), 7.26 (t, *J* = 7.5 Hz, 2H), 7.18 (t, *J* = 7.4 Hz, 2H), 6.70 (d, *J* = 8.9 Hz, 2H), 4.25 (d, *J* = 7.0 Hz, 2H), 4.18 (m, 1H), 4.04 (t, *J* = 6.9 Hz, 1H), 3.64 (s, 3H), 3.62 (s, 3H), 3.31 (m, 4H), 3.19 (s, 2H), 2.49 (t, *J* = 6.7 Hz, 1H), 2.33 (s, 2H), 1.95 (m, 2H), 1.62 (m, 4H), 1.39 (s, 9H), 1.03 (t, *J* = 7.0 Hz, 3H); ^{13}C NMR (151 MHz, MeOD) δ 177.2, 174.1, 173.6, 158.7, 157.7, 151.5, 150.5, 145.1, 144.4, 142.4, 141.1, 128.7, 128.1, 126.10, 126.07, 123.8, 121.1, 120.9, 112.3, 80.7, 67.6, 53.4, 52.7, 52.4, 50.5, 48.3, 46.2, 43.4, 39.3, 37.6, 34.7, 32.7, 28.7, 24.1, 12.7; HRMS (ESI+) *m/z* calcd for $C_{47}H_{57}O_9N_6$ $[M+H]^+$: 849.4182, found 849.4173; $[\alpha]_D$ = -10 (c = 0.9 in MeOH).

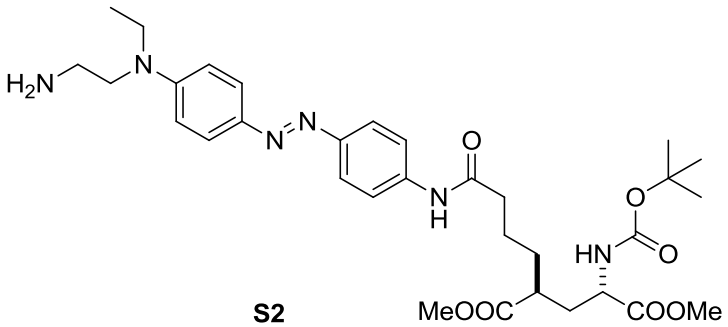

S2

Azobenzene S2. Azobenzene **S1** (214 mg, 0.252 mmol) was dissolved in THF (30 mL) and piperidine (0.25 mL, 2.52 mmol) was added. The reaction ran overnight but was not complete (as judged by TLC) so an additional volume of piperidine was added (0.5 mL, 5.04 mmol). After a further 5 h, the reaction was complete (by TLC). The reaction mixture was diluted with EtOAc and then extracted with a saturated

$NaHCO_3$ solution and brine; the organic phase was dried and concentrated. Column chromatography on silica gel (95:5:1 of CH_2Cl_2:MeOH:NEt_3) gave 149 mg (94%) of azobenzene **S2** as a red solid.

R_f 0.41 (10% MeOH in CH_2Cl_2, plus 1% NEt_3); ^{1}H NMR (600 MHz, MeOD) δ 7.78 (m, 4H), 7.70 (d, *J* = 8.6 Hz, 2H), 6.83 (d, *J* = 8.9 Hz, 2H), 4.18 (m, 1H), 3.69 (s, 3H), 3.67 (s, 3H), 3.56 (m, 1H), 3.48 (m, 2H), 3.35 (s, 1H), 2.99 (m, 2H), 2.52 (s, 1H), 2.39 (s, 2H), 1.97 (m, 2H), 1.65 (m, 4H), 1.42 (s, 9H), 1.17 (m, 3H); ^{13}C NMR (151 MHz, MeOD) δ 177.2, 174.2, 173.8, 157.8, 151.4, 150.5, 144.9, 141.3, 126.0, 123.8, 121.2, 112.8, 80.7, 54.7, 53.4, 52.7, 52.3, 50.9, 46.4, 43.5, 39.1, 37.6, 34.7, 32.7, 28.7, 24.1, 12.4; HRMS (ESI+) *m/z* calcd for $C_{32}H_{47}O_7N_6$ $[M+H]^+$: 627.3501, found 627.3500; $[\alpha]_D$ = -17 (c = 0.84 in MeOH).

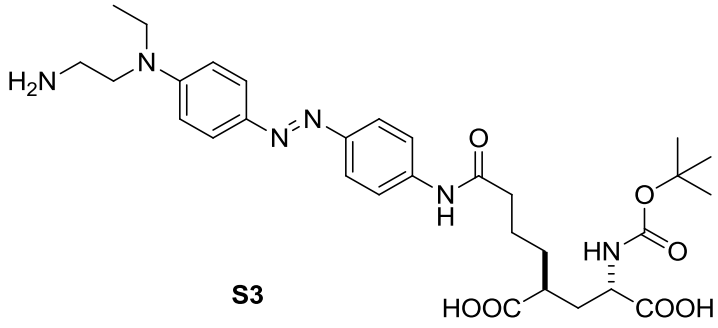

S3

Azobenzene S3. Azobenzene **S2** (149 mg, 0.237 mmol) was dissolved in THF (20 mL) and cooled in an ice bath to 0 °C, at which point an aqueous solution of LiOH (7 mL, 1 M) was added. The reaction was stirred at 0 °C for 1 h and then allowed to warm to rt while stirring for another 2 h. The reaction mixture was then acidified at 0 °C with formic acid and concentrated to remove the THF. The remaining aqueous solution was loaded onto a reverse phase column (gradient from 20% MeOH in 0.1% formic acid to 100% MeOH), giving 81 mg (57%) of azobenzene **S3** as a brown/yellow solid.

^{1}H NMR (600 MHz, MeOD) δ 8.32 (s, 1H), 7.82 (d, *J* = 8.6 Hz, 2H), 7.77 (d, *J* = 8.5 Hz, 2H), 7.70 (d, *J* = 8.4 Hz, 2H), 6.90 (d, *J* = 8.6 Hz, 2H), 4.14 (t, *J* = 7.6 Hz, 1H), 3.70 (t, *J* = 7.3 Hz, 2H), 3.55 (q, *J* = 7.1 Hz, 2H), 3.18 (t, *J* = 7.0 Hz, 2H), 2.53 (m, 1H), 2.42 (m, 2H), 1.96 (t, *J* = 7.4 Hz, 2H), 1.78 (m, 1H), 1.69 (m, 3H), 1.44 (s, 9H), 1.21 (t, *J* = 7.0 Hz, 3H); ^{13}C NMR (151 MHz, DMF) δ 177.0, 174.9, 163.6, 155.7, 150.2, 148.6, 143.7, 141.7, 124.9, 122.9, 119.5, 112.1, 78.2, 52.8, 47.2, 45.1, 42.3, 37.0, 35.2, 31.6, 28.0, 23.5, 11.8; HRMS (ESI+) *m/z* calcd for $C_{30}H_{43}O_7N_6$ $[M+H]^+$: 599.3188, found 599.3185; $[\alpha]_D$ = +40 (c = 0.3 in MeOH).

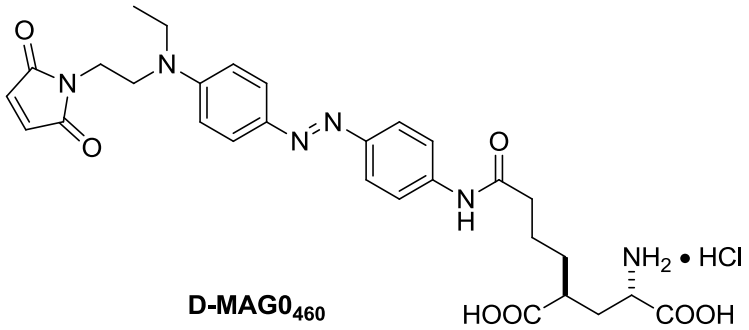

D-MAG0$_{460}$. Azobenzene **S3** (26.1 mg, 0.0436 mmol) was dissolved in a saturated aqueous solution of $NaHCO_3$ (2 mL) and cooled to 0 °C. N-methoxycarbonyl maleimide (33.8 mg, 0.218 mmol) was added, followed by THF (2 mL) 15 minutes later. The reaction was allowed to wam to rt and stirred another 1 h, at which point the reaction mixture was then acidified at 0 °C with formic acid and extracted three times with EtOAc, dried, and concentrated. Column chromatography on silica gel (5:95:1:1 MeOH:CH_2Cl_2:AcOH:H_2O, then 10:90:1:1 MeOH:CH_2Cl_2:AcOH:H_2O) gave 14.5 mg of a dark brown solid. This sensitive intermediate was then stirred in a saturated solution of HCl in dry EtOAc for 3 hours. Removal of solvent *in vacuo*, followed by three triturations with Et_2O and one with hexanes, gave 13.7 mg (51% over 2 steps) of **D-MAG0$_{460}$** as a dark purple, glassy solid.

^{1}H NMR (600 MHz, MeOD) δ 8.01 (d, *J* = 8.9 Hz, 2H), 7.80 (m, 4H), 7.19 (m, 2H), 6.82 (s, 2H), 3.99 (t, *J* = 7.1 Hz, 1H), 3.87 (m, 4H), 3.75 (m, 2H), 2.80 (m, 1H), 2.47 (m, 2H), 2.17 (m, 1H), 2.05 (m, 1H), 1.77 (m, 4H), 1.31 (m, 3H); ^{13}C NMR (151 MHz, DMF) δ 176.8, 172.7, 172.2, 171.9, 151.2, 149.4, 144.4, 142.7, 135.8, 125.9, 123.7, 120.4, 112.7, 52.3, 49.9, 48.7, 46.0, 41.8, 37.6, 33.5, 32.4, 23.9, 12.9; HRMS (ESI+) *m/z* calcd for $C_{29}H_{35}O_7N_6$ $[M+H]^+$: 579.2562, found 579.2561; $[\alpha]_D$ = -6 (c = 0.7 in MeOH).

Supporting Results

S1. Measurement and analysis of 2P absorption spectra. 2P absorption is a third-order nonlinear process that depends on both the 2-photon absorption cross-section (σ_2) and the squared concentration of incident photons. As noted by Xu and Webb (7), accurate measurement of 2P absorption spectra depends strongly on spatial and temporal properties of the laser field, E(z,ω,t). Differences in laser conditions can lead to very different reported values for σ_2, making it difficult to compare materials, or even the relative strength of transitions within a material. We sought to avoid many of these complications by making simultaneous measurement of 2P absorption over a broad range of transition energies using a non-degenerate (*2-color*) white light spectrophotometry method (8–10). This nonlinear spectrophotometry technique uses the same experimental apparatus as femtosecond transient absorption (Fig. S2a), where the pump-dependent change in absorption for a weak probe pulse, E(ω), has been described theoretically in terms of the third-order polarization response (11, 12):

$$\Delta A(\omega) \sim \omega \, \mathrm{Im} \frac{\mathbf{P}^{(3)}(\omega)}{\mathbf{E}(\omega)} \tag{1}$$

In contrast to transient absorption, for the 2-color-2P absorption measurement, pump and probe pulses are detuned from the 1-photon absorption spectrum of the photoswitch (Fig. S2b). Under these conditions, changes in probe transmission are observed only when the pulses are temporally overlapped. Neither beam has sufficient energy or intensity to excite a photoisomerization independently, as confirmed by the lack of a persistent bleach of the initial isomer (Fig. S2c). The third-order polarization response seen by the probe pulse can be written:

$$\mathbf{P}^{(3)}(\omega) \cong \chi^{(3)}(\omega = \omega_{NIR} + \omega - \omega_{NIR}) \, \mathbf{E}(\omega)\mathbf{E}_{NIR}(\omega_{NIR})\mathbf{E}_{NIR}(\omega_{NIR}) \tag{2}$$

Two types of phenomena contribute to Eq. 2: (1) absorption that occur when photons from both laser pulses interact with the same molecule, including both 2P absorption and stimulated Raman scattering; (2) cross-phase modulation of E(ω,t) by the pump $|E_{NIR}(\omega_{NIR}, t)|^2$. The latter signal predominantly arises from the $\chi^{(3)}$ properties of the solvent and cuvette windows. It can be seen from measurements in the absence of a 2P absorber (either in transparent solvent or in empty cuvette), that the cross-phase modulation signal has a time-integral equal to zero and does not contribute to Eq. 1, and therefore can be subtracted from the signal measured in the PTL sample if conditions are identical. Comparing the sample and solvent measurements yields a spectrally-resolved measure of the $\chi^{(3)}$ contribution of the sample:

$$\Delta A(\omega) = \Delta A_{sample} - \Delta A_{solvent} = \left[\omega \, \mathrm{Im} \frac{\mathbf{P}^{(3)}(\omega)}{\mathbf{E}(\omega)}\right]_{sample} - \left[\omega \, \mathrm{Im} \frac{\mathbf{P}^{(3)}(\omega)}{\mathbf{E}(\omega)}\right]_{solvent} \tag{3a}$$

$$\Delta A(\omega) = \chi^{(3)}(\omega)\mathbf{E}_{NIR}(\omega_{NIR})\mathbf{E}_{NIR}(\omega_{NIR}) \propto c \, \sigma_2(\lambda) \, I_{NIR} \tag{3b}$$

Note that Eq. 3b is linear in NIR intensity. From Eq. 3b, two samples measured under identical conditions, a ratio of $\Delta A(\lambda_{WL}, \lambda_{NIR})$ measurements is sufficient to determine a relative 2P cross-section without knowledge of the exact spatial and temporal properties of I_{WL} and I_{NIR}. The unknown cross-section $\sigma_2(\lambda)$ is given by:

$$\sigma_2(\lambda) = \frac{\Delta A}{\Delta A^{ref}} \frac{C^{ref}}{C} \sigma_2(\lambda)^{ref} \quad (4)$$

For measurement of photoswitches, back-to-back measurements were made in neat solvent in the same sample cuvette to verify cancellation of cross-phase modulation and identify contributions to ΔA_{WL} not due to 2P absorption (Figs. S3, S4, S5). Laser parameters for 2P absorption measurements are summarized in Table S1. For measurements with λ_{NIR} = 1360 nm, we used coumarin 153 in methanol as a reference sample, with a reported σ_2 = 45 GM (7); for measurements where λ_{NIR} = 800 nm, we used MNI-glutamate in water, with a reported σ_2 = 0.04 ± 0.02 GM at 730 nm (13). Spectroscopic parameters for reference samples are summarized in Table S2. In the measured spectrum of L-MAG0, we observe an absorption feature at λ = 360 nm (Fig. S3g). Upon analysis, this is seen to correspond to Raman scattering of the 800 nm pulse by the 2994, 2913 cm^{-1} CH stretching modes of DMSO (14) (Fig. S3h). The peaks remaining after solvent corrections can be attributed to Raman scattering from the azobenzene moiety (Fig. S3h).

We also measured the 2P absorption of another first-generation PTL, maleimide-azobenzene-quaternary ammonium (MAQ) (15, 16) in phosphate buffered solution (Figure S4). Despite a bathochromatic shift in the near-UV π-π* absorption band (λ_{1P} = 360 nm in phosphate buffered solution, pH 7.4), the 2P absorption of *trans*-MAQ was very similar to *trans*-L-MAG0 (Fig. 1a). The lack of a solvent shift supports the interpretation that the absorption peak at 318 nm is not due to vibronic enhancement within the lowest energy π-π* transition, but rather corresponds to a different electronic transition. Considering that the *trans*-MAQ measurement used a different combination of white light and NIR wavelengths (Figure S4b), we also saw no evidence that these σ_2 spectra were grossly influenced by resonance-enhanced 2P absorption due to overlap between the white light and 1P absorption spectra.

S2. Photoisomerization dynamics in MAGs. The photoisomerization model for 400 nm excitation of L-MAG0 and L-$MAG0_{460}$ was based on *trans*-azobenzene, as shown in Figure S6. Photoexcitation promotes molecules from the dark-equilibrated *trans* (E) isomer ground state to the first 1P-allowed (S_2) excited state, where relaxation occurs through internal conversion with an effective time constant τ_1 = 130 fs. Approximately 45% of photoexcited molecules relax to an S_1 excited state where they structurally evolve away from the Frank-Condon region with τ_{FC}. Isomerization occurs from S_1, resulting in a net quantum yield for the *cis* isomer of 0.15 in L-MAG0. Failed isomerization attempts result in a vibrationally excited *trans* population that thermally equilibrates with τ_{vib}. In L-$MAG0_{460}$, the n-π and π-π* transitions are inverted and the entire photoexcited population goes through S_1, resulting in a higher yield of *cis* photoproduct ($\phi^{E\rightarrow Z}$ = 0.4). Time constants are summarized in Table S3, where the effective rate constants (τ_1, τ_2) are related to Figure S6 by $(\tau_1)^{-1} = k_{20} + k_{21}$ and $(\tau_2)^{-1} = k_{10} + k^{E\rightarrow Z}$, and $\tau_{FC} = (k_{21})^{-1}$. All values have an error of ± 10%.

S3. Relationship of L-MAG0$_{460}$ photocurrent kinetics to photoswitching. Since the photoactive effects of PTLs (e.g., LiGluR photocurrents controlled by MAGs) are reversibly triggered by *trans* → *cis* isomerization (denoted as E-Z) and turned off by *cis* → *trans* isomerization (Z-E). If we assume that instantaneous photocurrent can be approximated by the concentration of *cis* isomer [Z], modulo an efficiency factor η_γ, then the current can modeled by rate equations for a unimolecular reaction, where k_{KT} is the rate constant for thermal isomerization and the rate constants k_γ represent photoisomerization for γ-photon absorption (γ = 1,2):

$$\frac{dS}{dt} \approx \eta_\gamma \frac{d[Z]}{dt} \tag{5a}$$

$$\frac{d[Z]}{dt} = k_\gamma^{E\to Z}[E] - k_\gamma^{Z\to E}[Z] - k_{KT}[Z] \tag{5b}$$

The LiGluR + L-MAG0$_{460}$ photocurrent dark relaxation kinetics were presumably rate-limited by thermal relaxation of the *cis* isomer, as described previously (6). We can readily observe from the recordings in Figure 4 that, at the light intensities of the experiment (1P: 0.02 – 0.26 μW^2/μm^2 = 0.6 – 8.7 x 10^{19} γ s^{-1}cm^{-2}; 2P: 0.3 – 2.3 mW^2/μm^2 = 1.2 – 9.5 x 10^{23} γ s^{-1}cm^{-2}), photoisomerization rates (k_γ) were collectively much faster than k_{KT} for both 1P and 2P LiGluR photocurrents. Therefore, we estimate that LiGluR currents saturate as a *photostationary* state (PSS) is reached:

$$S_{max} \approx \eta_\gamma [Z]_{PSS} = \eta_\gamma \frac{k_\gamma^{E\to Z}}{k_\gamma^{Z\to E}} [E]_{PSS} \tag{6}$$

Eq. 6 predicts that S_{max} should be independent of light intensity for a given cell. Although S_{max} varied widely between cells, we can still say something about relative photocurrent, s(t) = S(t)/S_{max}, in terms of fractional population [Z]:

$$\frac{ds}{dt} = k_\gamma^{E\to Z}(1 - [Z]) - k_\gamma^{Z\to E}[Z] \tag{7}$$

The rate constants for photoisomerization depend on the light intensity-dependent rate of absorption and reaction quantum yield:

$$k(\lambda)_\gamma^{E\to Z} = \frac{1}{\gamma} \Phi_\gamma^{E\to Z} \sigma(\lambda)_\gamma^E \, I(\lambda)^\gamma \tag{8a}$$

$$k(\lambda)_\gamma^{Z\to E} = \frac{1}{\gamma} \Phi_\gamma^{Z\to E} \sigma(\lambda)_\gamma^Z \, I(\lambda)^\gamma \tag{8b}$$

where $\sigma(\lambda)_\gamma$ is the γ-photon absorption cross-section, and I(λ) is the light intensity in units γ s^{-1}cm^{-2}. Combining Eqs. 7 and 8, the rate at which S_{max} is approached is:

$$\frac{ds}{dt} = -\frac{\eta_\gamma}{\gamma}\left[\Phi_\gamma^{E\to Z}\sigma(\lambda)_\gamma^E + \Phi_\gamma^{Z\to E}\sigma(\lambda)_\gamma^Z\right] \; I(\lambda)^\gamma \, [Z] + \eta_\gamma k_\gamma^{E\to Z} \tag{9}$$

The solution to Eq. 9 is a decaying exponential with rate constant:

$$k_{on} = \frac{\eta_\gamma}{\gamma} \left[\Phi_\gamma^{E\to Z} \sigma(\lambda)_\gamma^E + \Phi_\gamma^{Z\to E} \sigma(\lambda)_\gamma^Z \right] \; I(\lambda)^\gamma \tag{10}$$

Eq. 10 predicts that the rate of photocurrent onset under saturation conditions should depend on light intensity linearly for 1P photoswitching, and as I^2 for 2P photoswitching.

Experimentally, the photocurrent rise for 1P excitation was well fit by a single exponential. By measuring the rise time for several light intensities in the same cell, we found that the rates constant showed a linear relationship with light intensity (Fig. S7c). A minimum intensity of 0.1 μW/μm^2 produced a steady state photocurrent indicative of equilibrium between *trans* → *cis* and *cis* → *trans* isomerization rates. Across cells, 470 nm light of intensity 0.36 μW/μm^2 yielded an average τ_{on} = 4.6 ± 0.4 ms, while 2P-DH photocurrents had an average τ_{on} = 11.5 ± 2.4 ms (Fig. S7b). For most cells, the on-rates for 2P photoactivation was sufficient to reach a steady state current (Fig. S7b) with 2P intensities tolerated by healthy neurons (290 ± 10 mW time-averaged power distributed into 130-300 μm^2 regions). Cell "tolerance" was judge by stability over repeated photoswitching cycles (representative examples after 30 cycles shown in Fig. 4a, b). We conclude that 2P photoactivation of LiGluR + L-MAG0$_{460}$ is efficient enough to generate maximum current density without cell damage.

As noted by Rickgauer and Tank for Channelrhodopsin2 (17), photocurrent kinetics can provide complementary quantitative measures of spectroscopic values given a model relating photophysics to physiological mechanism. They developed a framework relating the ChR2 photocycle to photocurrents measured *at saturation*, and based on fitting experimental functional data determined a value of σ_2 for ChR2 (260 ± 20 GM at 920 nm). Although the origin of photocurrent saturation in ChR2 is a thermodynamic photocycle rather than photochromism, a similar type of framework can be extended to photochromic PTLs through the photostationary model described above. In fact, using the experimental values for brightness in Eq. 10, we obtain intensity-dependence rate constants that agree well with the photocurrent rise times measured in neurons with LiGluR (Fig. S7f, dashed = predicted, symbols = experimental), assuming an efficiency factor $\eta_1 = \eta_2 = 0.1$, and that the 2P absorption of *cis*-L-MAG0$_{460}$ follows the 1P absorption (as in *cis*-L-MAG0).

S4. Interpretation of LimGluR-dependent photocurrents. LimGluR3 + D-MAG0$_{460}$-dependent GIRK current had considerably different kinetics than LiGluR photocurrents, despite the chemical similarity of L-MAG0$_{460}$ and D-MAG0$_{460}$. These differences can be attributed to the nature of LimGluR and the indirect readout of LimGluR activity (Figure S8). Considering that similar excitation intensities produced a photostationary *cis* population in LiGluR + L-MAG0$_{460}$ (Figure 4), the slower onset LimGluR3 + D-MAG0$_{460}$ photoactivation suggests that G protein signaling is rate-limiting, or possibly that second messenger recruitment to LimGluR3 competes with thermal relaxation of D-MAG0$_{460}$.

References

1. Szobota S, et al. (2007) Remote control of neuronal activity with a light-gated glutamate receptor. *Neuron* 54(4):535–545.

2. Weston MC, Gertler C, Mayer ML, Rosenmund C (2006) Interdomain Interactions in AMPA and Kainate Receptors Regulate Affinity for Glutamate. *J Neurosci* 26(29):7650–7658.

3. Zhao Y, et al. (2011) An Expanded Palette of Genetically Encoded Ca2+ Indicators. *Science* 333(6051):1888–1891.

4. Gottlieb HE, Kotlyar V, Nudelman A (1997) NMR Chemical Shifts of Common Laboratory Solvents as Trace Impurities. *J Org Chem* 62(21):7512–7515.

5. Levitz J, et al. (2013) Optical control of metabotropic glutamate receptors. *Nat Neurosci* 16(4):507–516.

6. Kienzler MA, et al. (2013) A Red-Shifted, Fast-Relaxing Azobenzene Photoswitch for Visible Light Control of an Ionotropic Glutamate Receptor. *J Am Chem Soc* 135(47):17683–17686.

7. Xu C, Webb WW (1996) Measurement of two-photon excitation cross sections of molecular fluorophores with data from 690 to 1050 nm. *J Opt Soc Am B* 13(3):481–491.

8. Negres RA, Hales JM, Kobyakov A, Hagan DJ, Van Stryland EW (2002) Two-photon spectroscopy and analysis with a white-light continuum probe. *Opt Lett* 27(4):270–272.

9. He G, et al. (2002) New technique for degenerate two-photon absorption spectral measurements using femtosecond continuum generation. *Opt Express* 10(13):566–574.

10. Yamaguchi S, Tahara T (2003) Two-photon absorption spectrum of all-trans retinal. *Chem Phys Lett* 376(1–2):237–243.

11. Mukamel S (1983) Nonimpact unified theory of four-wave mixing and two-photon processes. *Phys Rev A* 28:3480–3492.

12. Pollard WT, Mathies RA (1992) Analysis of Femtosecond Dynamic Absorption Spectra of Nonstationary States. *Annu Rev Phys Chem* 43(1):497–523.

13. Trigo FF, Corrie JET, Ogden D (2009) Laser photolysis of caged compounds at 405 nm: photochemical advantages, localisation, phototoxicity and methods for calibration. *J Neurosci Methods* 180(1):9–21.

14. Martens WN, Frost RL, Kristof J, Theo Kloprogge J (2002) Raman spectroscopy of dimethyl sulphoxide and deuterated dimethyl sulphoxide at 298 and 77 K. *J Raman Spectrosc* 33(2):84–91.

15. Banghart M, Borges K, Isacoff E, Trauner D, Kramer RH (2004) Light-activated ion channels for remote control of neuronal firing. *Nat Neurosci* 7(12):1381–1386.

16. Fortin DL, et al. (2008) Photochemical control of endogenous ion channels and cellular excitability. *Nat Methods* 5(4):331–338.

17. Rickgauer JP, Tank DW (2009) Two-photon excitation of channelrhodopsin-2 at saturation. *Proc Natl Acad Sci* 106(35):15025–15030.

18. Fischer A, Cremer C, Stelzer EH (1995) Fluorescence of coumarins and xanthenes after two-photon absorption with a pulsed titanium-sapphire laser. *Appl Opt* 34(12):1989–2003.

19. Brackmann U (2000) Lambdachrome Laser Dyes.

20. Makarov NS, Drobizhev M, Rebane A (2008) Two-photon absorption standards in the 550-1600 nmexcitation wavelength range. *Opt Express* 16(6):4029–4047.

Supporting Figure Legends

Figure S1. Visible absorption of L-MAG0$_{460}$ is composed of two overlapping bands. The *trans*-L-MAG0$_{460}$ 1P absorption spectrum in DMSO and water can be decomposed in two absorption bands. The larger solvent shift of the lower energy band is consistent with a π-π^* transition, suggesting an inversion of the transition energies.

Figure S2. Femtosecond spectrophotometry. (a) Block diagram of optical setup for broadband femtosecond pump-probe spectroscopy: WLG, white light generation; SHG, second-harmonic generation in BBO. The optical path length between pump and probe pulses is varied with a computer-controlled translation stage. At each delay point, the pump beam is blocked with an optical chopper and the transmission spectrum of the white light pulse is collected with and without pump exposure. Difference spectra are calculated as $\Delta A(\lambda, t) = -\log [I(\lambda,t)_{pump} / I(\lambda)_{no\ pump}]$. (b) Transient absorption, the pulse wavelengths are selected to be sensitive to photo-excited changes in electronic states. Nonlinear optical effects are frequently observed in pump-probe measurements in the brief period when the pump and probe pulses are coincident (TIME-ZERO). Though sometimes called a "coherent artifact" in transient absorption spectroscopy, this two color interaction can be exploited for measurement of two-photon absorption (right). (c) Example of time- and wavelength-resolved ΔA data. Note the x-axis is logarithmic for values past 1 ps. Following the pump pulse, ΔA dynamics result from the relaxation of non-equilibrium populations; the formation of stable photoproducts causes a persistent ΔA. (d) Example of time- and wavelength-resolved ΔA data for 2-color 2P absorption measurement. Note that no signal persists past "TIME-ZERO".

Figure S3. Anatomy of the 2P absorption measurement. (a) 2P absorption can involve two photons with *degenerate* properties (necessarily half the electronic transition energy), or *non-degenerate* photon pairs that summate to the transition energy. Non-resonant photons must interact with the same molecule within the lifetime of virtual transition states (dashed lines) for 2P absorption. (b) *Non-degenerate* 2P absorption spectra was measured using the nonlinear spectrophotometer described in Figure S2, where pump and probe wavelengths were detuned from the PTL 1P absorption. The white light (WL) probe was tuned to longer wavelengths, while the resonant pump pulse was replaced with a non-resonant NIR pulse so that WL and NIR energies summate to the transition energy. (c) Changes in white light are induced by the NIR pulse, but unlike a transient absorption measurement, no measurable excited state population is generated and $\Delta A(\lambda_{WL})$ returns to baseline. (d) The ΔA signal has contributions from cross-phase modulation (XPM) and 2P absorption. Viewed as time-resolved spectra (shown at 150 fs intervals), XPM is seen as loss ($\Delta A(\lambda_{WL}) > 0$) in the center wavelength and gain ($\Delta A(\lambda_{WL}) < 0$) at new wavelengths generated as the nonlinear field of the NIR pulse changes the instantaneous frequency of the white light. XPM is nearly identical in back-to-back measurements of PTL (solid lines) and neat solvent (dashed lines). The difference represents the contribution due to 2P absorption of the PTL. (e) The measurement has better than 400 cm^{-1} spectral resolution. (f) Viewed in the time domain, the cross-correlation of WL and NIR pulses is ≈150 fs. (g) The time-integrated $\Delta A(\lambda_{WL})$ signal is directly proportional to 2P absorption. The signal in solvent confirms that XPM contributes no net loss of probe light. (h) Anti-Stokes Stimulated Raman scattering of λ_{NIR} = 800 nm by the 2994, 2913 cm^{-1} CH stretching modes of DMSO was stimulated

by the white light probe and appears as a positive signal in the time-integrated ΔA signal for neat DMSO (black) and L-MAG0 in DMSO (red = trans, green = cis). (h) The peaks remaining after solvent corrections can be attributed to Raman scattering from the azobenzene moiety. (i) For the wavelength combination in panel b, we used MNI-glutamate as the reference sample with known 2P cross-section. Red symbols are the 2P absorption signals scaled to reported σ_2 values. The 1P absorption spectrum is shown for reference (blue lines).

Figure S4. 2P absorption of MAQ. (a) 2P absorption spectrum of a related first generation PTL, maleimide-azobenzene-quaternary ammonium (MAQ) (15, 16) was very similar to that of *trans*-L-MAG0 (Fig. 1a). The lack of a solvent shift supports the interpretation that the absorption peak at 318 nm is not a vibronically-enhanced π-π* transition, but rather corresponds to a different electronic transition. (b) The *trans*-MAQ measurement used a different combination of white light and NIR wavelengths. (c) Dispersion of WL probe. (d) Time-resolved difference spectra at 100-fs intervals give an estimate of spectral resolution. Cross-correlation signals were measured in neat solvent (dashed) to identify contributions from cross-phase modulation and Raman scattering.

Figure S5. 2P absorption of L-MAG0$_{460}$ and reference spectra. (a) Overlap of WL probe spectrum with L-MAG0$_{460}$ and L-MAG0 was minimized. (b) Evaluation of 2P spectra was limited to use only the spectral region where the WL probe was linearly chirped (λ < 650 nm). (c) Time-resolved difference spectra at 100 fs intervals in DMSO give an estimate of spectral resolution. (d) The time-integrated $\Delta A(\lambda_{WL})$ signal is directly proportional to 2P absorption. The signal in solvent confirms that XPM contributes no net loss of probe light. Some resonance-enhanced 2P absorption (denoted with **) was observed on the high-energy side of L-MAG0$_{460}$ spectrum where there is greatest overlap between the WL and MAG 1P absorption. (e) The reference spectrum for this combination of wavelengths was coumarin 153 in methanol. Red symbols are the 2P absorption signals scaled to reported σ_2 values. The 1P absorption spectrum is shown for reference (blue lines).

Figure S6. Photoisomerization dynamics in MAGs. (a) Heat map representation of time-resolved changes in absorption during trans-cis photoisomerization reaction in L-MAG0. The x-axis is linear until 1 ps, and logarithmic thereafter. (b) Photoisomerization model for 400 nm excitation of L-MAG0: The π-π* transition in dark-equilibrated *trans* (E) isomer promotes molecules to the S_2 excited state, where they relax through internal conversion with an effective time constant τ_1 = 130 fs. Approximately 45% of photoexcited molecules relax to an S_1 excited state where they structurally evolve away from the Frank-Condon region with τ_{FC}. Isomerization occurs from S_1, resulting in a net quantum yield for the *cis* isomer. Failed isomerization attempts result in a vibrationally excited *trans* population that thermally equilibrates with τ_{vib}. (c) Kinetics at various probe wavelengths show the simplicity of the photodynamics. (d) Time-resolved spectra at select probe delays. (e) Concentrations of state populations obtained global analysis with the target model depicted in panel b. (f) Species Associated Difference Spectra (SADS) show the net wavelength-dependence of the exponential time constants (Table S3). (g) Heat map representation of transient absorption during *trans*-L-MAG0$_{460}$ photoreaction. (h) 400 nm directly excites molecules to the photoisomerization intermediate state because of the inversion of transition energies. (i) Kinetics at various probe wavelengths show slightly more complex photodynamics than in L-MAG0. (j) Time-resolved

spectra at select probe delays. (k) Concentrations of state populations obtained global analysis with the target model depicted in panel h. (l) Species Associated Difference Spectra (SADS) show the net wavelength-dependence of the exponential time constants. The vibrationally excited population (blue, green lines) equilibrate within ~15 ps to a bleach spectrum that matches the ground state absorption spectrum.

Figure S7. Stationary state photocurrents in LiGluR + L-MAG0$_{460}$. (a) Neuronal LiGluR photocurrents showed no correlation between maximum photocurrent amplitude and rate constant of photocurrent onset ($k_{on} = \tau_{on}^{-1}$). (b) Comparison of τ_{on} for 1P and 2P photocurrents from Figure 4 with 1P power series measured within individual cells (1**). (c) Intensity-dependence of 1P photocurrents recorded from single cells. An intensity of ≈ 0.1 μW/μm^2 produced a steady state photocurrent that could be sustained for the duration of light pulse. (d) k_{on} showed a linear dependence on light intensity. (e) Example of 2P photocurrent elicited by 2P-DH time-averaged intensity of 1.8 ± 0.3 mW/μm^2 at 850 nm. (f) The measured rate constants (symbols) are consistent with predicted values predicted by the PSS model (Eq. 10) using the experimental values for 1P and 2P brightness and an efficiency factor, η = 0.1.

Figure S8. GPCR signaling is rate-limiting step in photoagonism of LimGluR3 by D-MAG0$_{460}$. (a) The LimGluR3 + D-MAG0$_{460}$-dependent GIRK current increased steadily with light exposure, approaching a maximum steady state after 5-8 s at 0.4 μW/μm^2. Well below this intensity, LiGluR + L-MAG0$_{460}$ photocurrents reached stationary state within 100 ms (Fig. S7). (b) Intensity dependence of LimGluR3 + D-MAG0$_{460}$ signal recorded from a single cell. (c) The rate constant of GIRK current rise, measured here as the time to reach 90% of the current at 5 s, did not depend on intensity (n=3 cells, at least 3 intensities tested per cell).

Proton NMR spectra of new compounds.

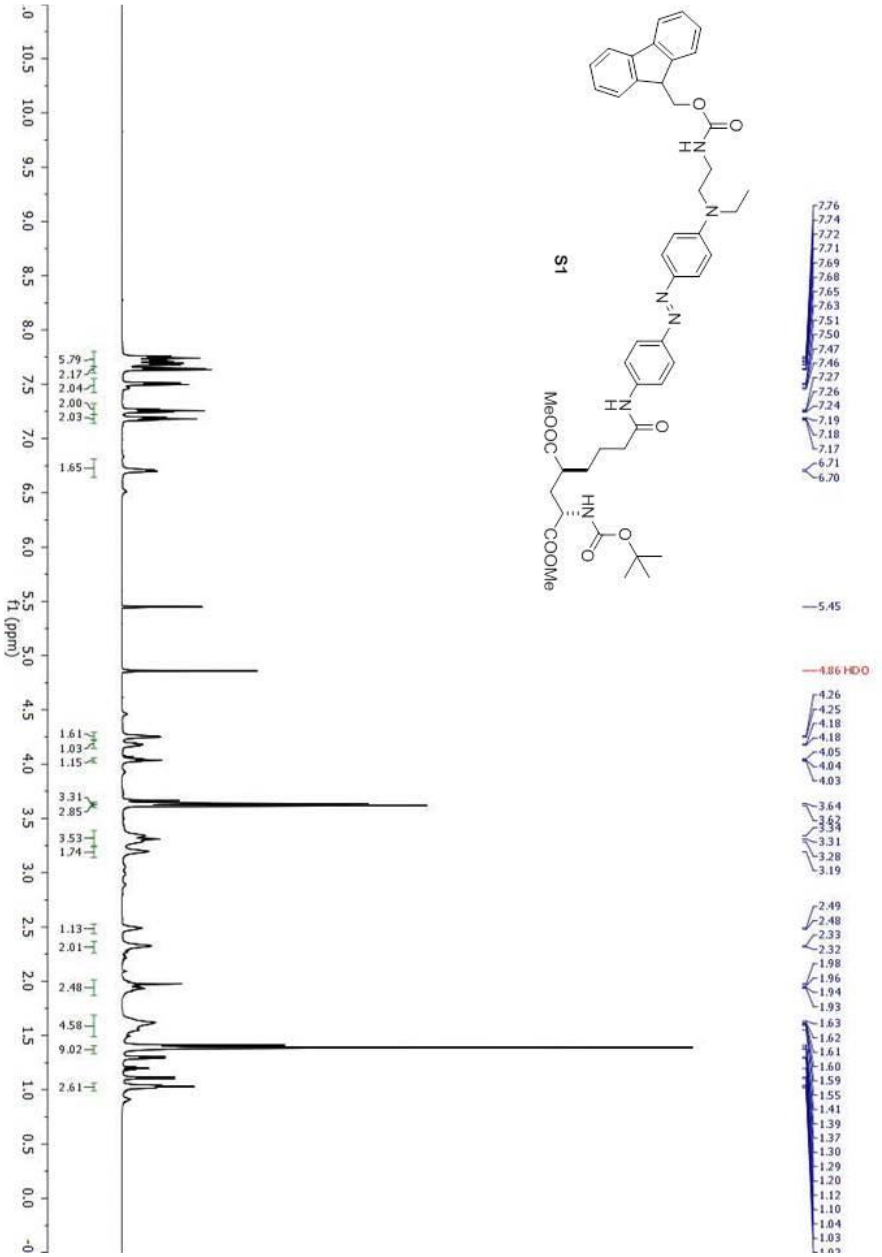

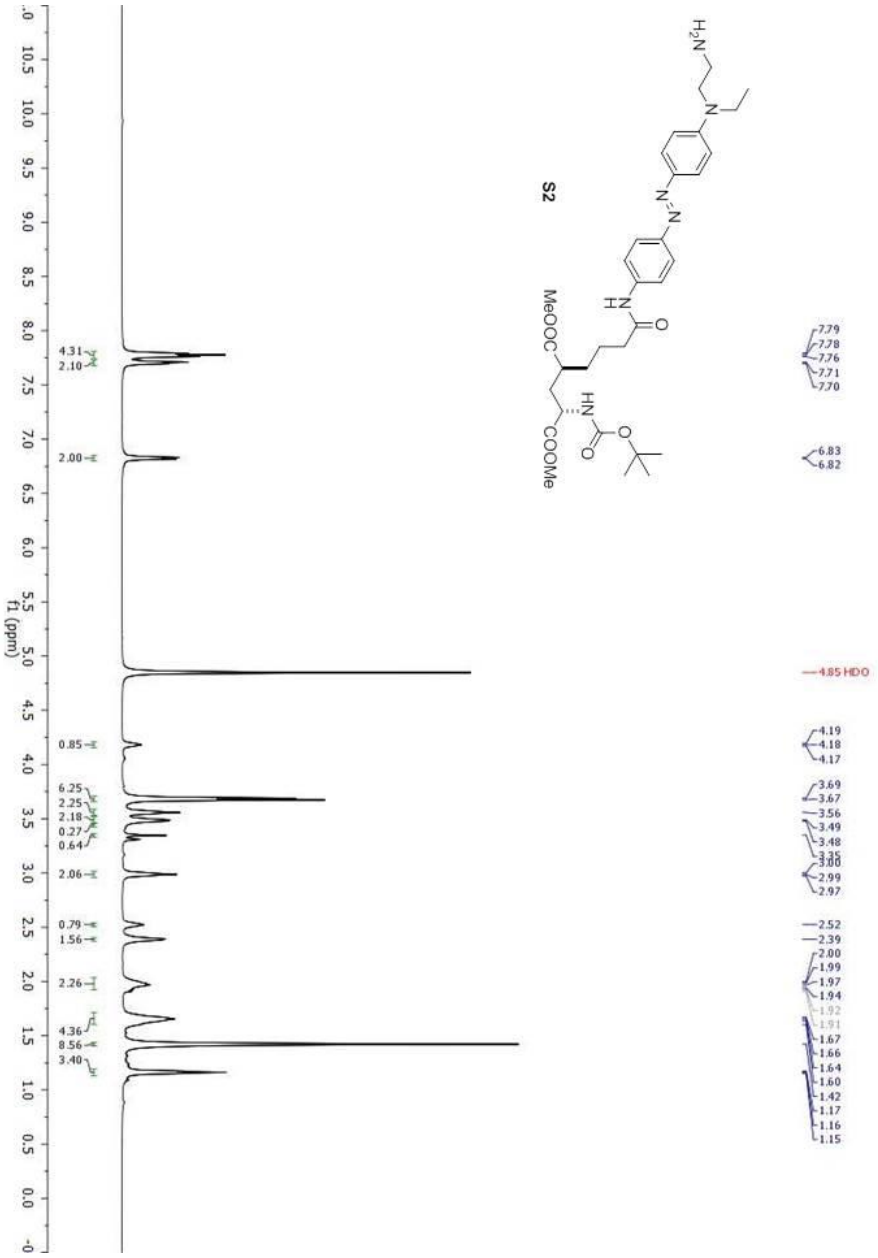
S2
MeOOC
COOMe
f1 (ppm)
4.85 HDO

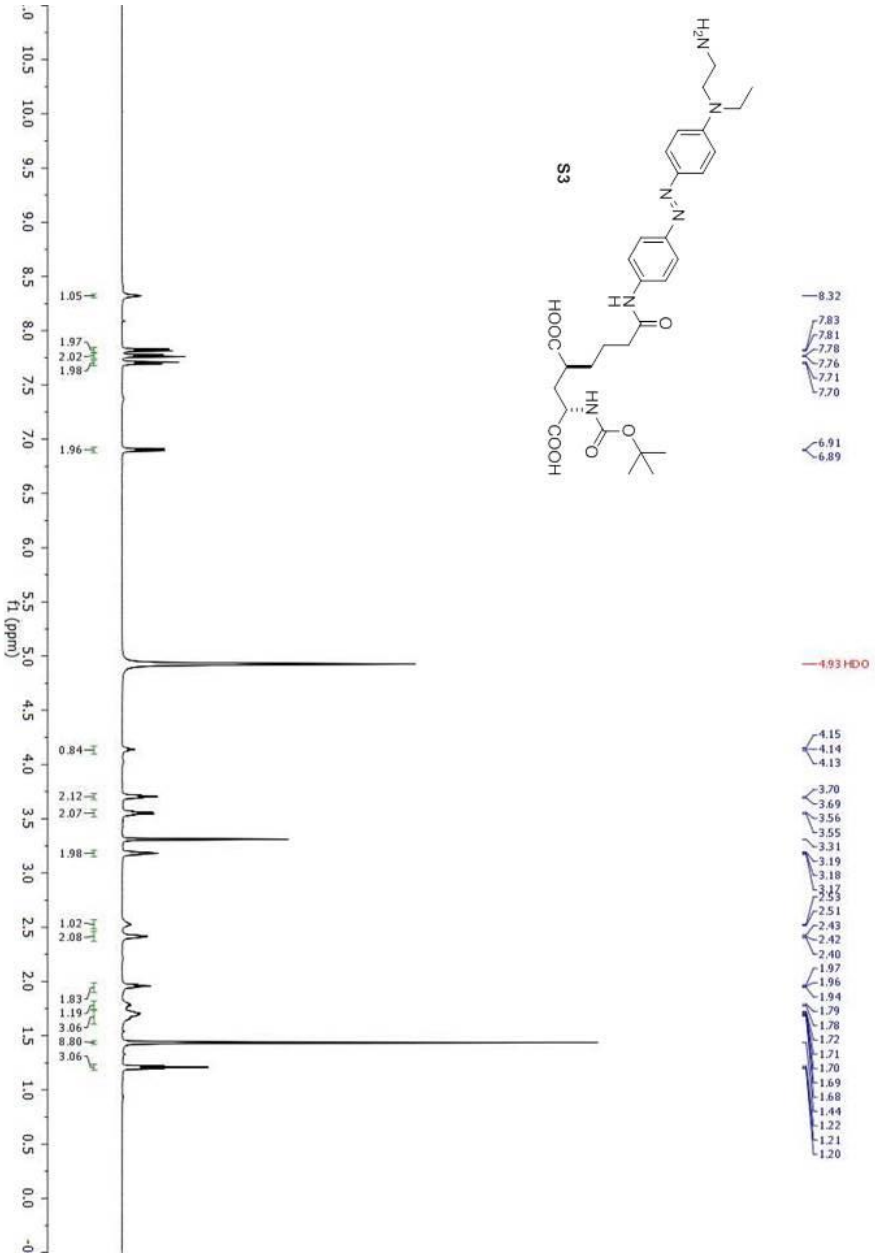
S3
f1 (ppm)
4.93 HDO

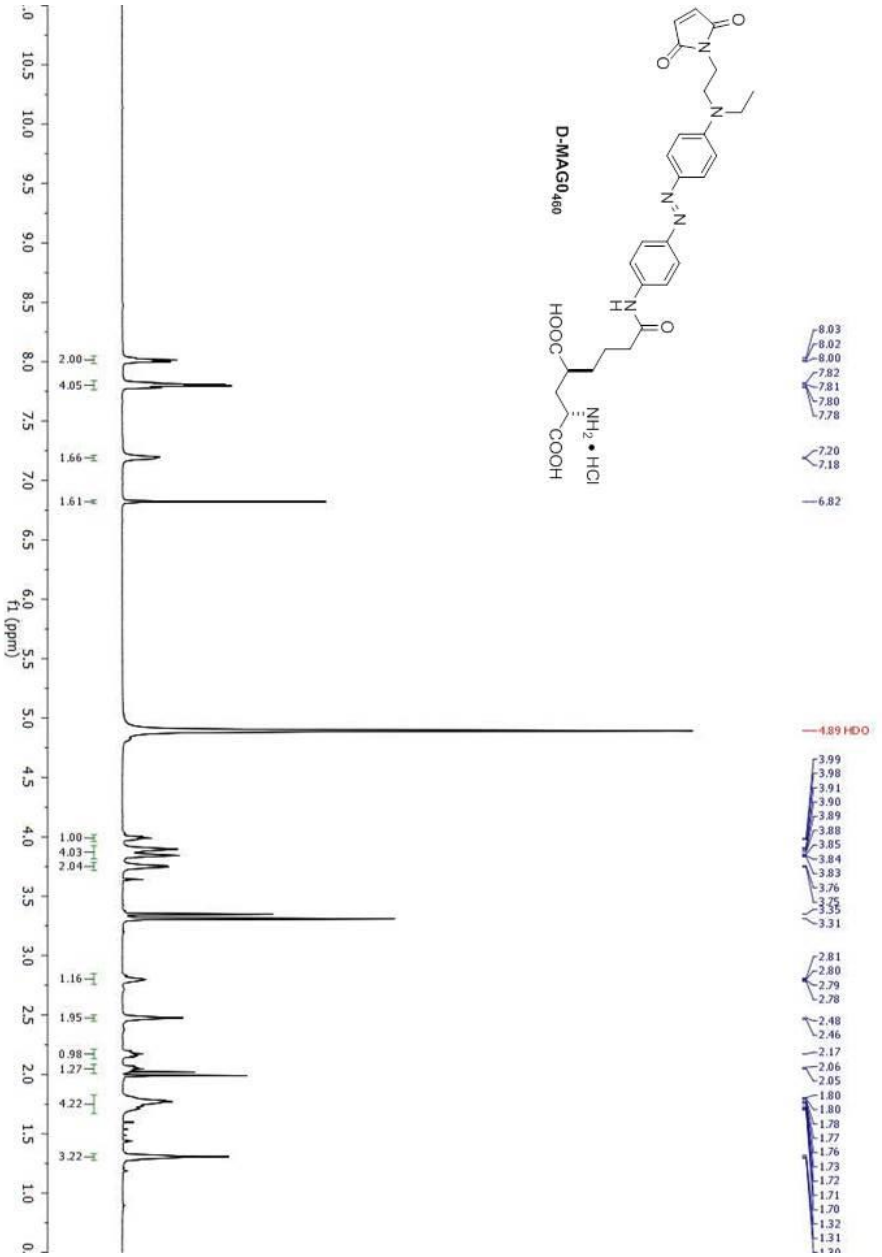
D-MAG0460
HOOC
NH2 • HCl
COOH
f1 (ppm)
4.89 HDO

Table S1. Summary of laser conditions used in 2P absorption measurements.

PTL	λ_{NIR} (nm)	WL medium	λ_{eff} (nm)	Reference
MAQ	1420	CaF_2	300-450	--
L-MAG0$_{460}$ L-MAG0	1360	Sapphire	400-450	Coumarin 153
L-MAG0	800	YAG	300-375	MNI-glutamate

Table S2. Summary of reference absorption values.

	Units	MNI-glutamate	Coumarin 153
solvent		DI, pH 7.0	MeOH
λ_{max}	nm	336[a]	423[b]
E	$M^{-1}cm^{-1}$	4820 (13)	14700†
2λ	nm	730[a]	800[c]
σ_2	GM	0.04 ± 0.02	45 ± 7

[a] Reference (13).

[b] Reported extinction coefficients at 423 nm: ε = 14700 $M^{-1}cm^{-1}$ in MeOH(18), ε = 18900 $M^{-1}cm^{-1}$ in EtOH (19).

[c] Reference (20).

Table S3. Fitted parameters for MAG photoisomerization in DMSO.

PTL	λ_{pump} (nm)	τ_1 (ps)	τ_{FC} (ps)	τ_2 (ps)	$(k^{e-z})^{-1}$ (ps)	τ^e_{vib} (ps)	τ^z_{vib}	$\phi^{e\rightarrow z}$
L-MAG0	400	0.13	0.4	0.6	2.4	12	--	0.11
L-MAG0$_{460}$	400	--	0.2	0.6	2	15	3	0.4
L-MAG0$_{460}$	800	--	n.d.	n.d.	2	15	3	0.4

n.d., not determined.

Carroll_Figure S1

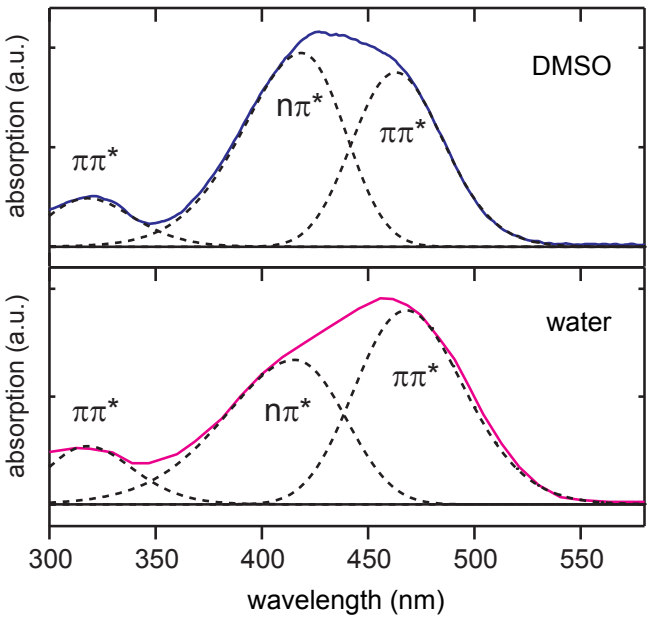

Carroll_Figure S2

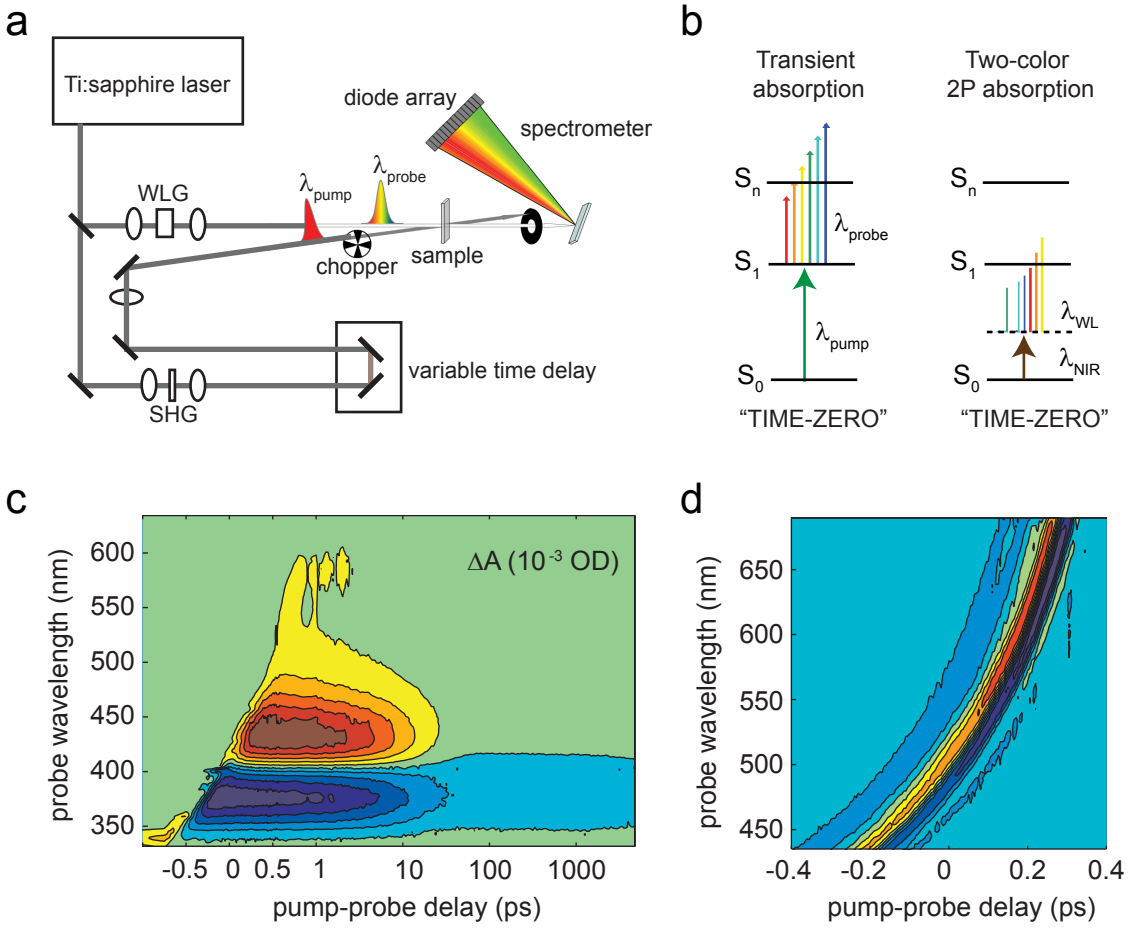

Carroll_Figure S3

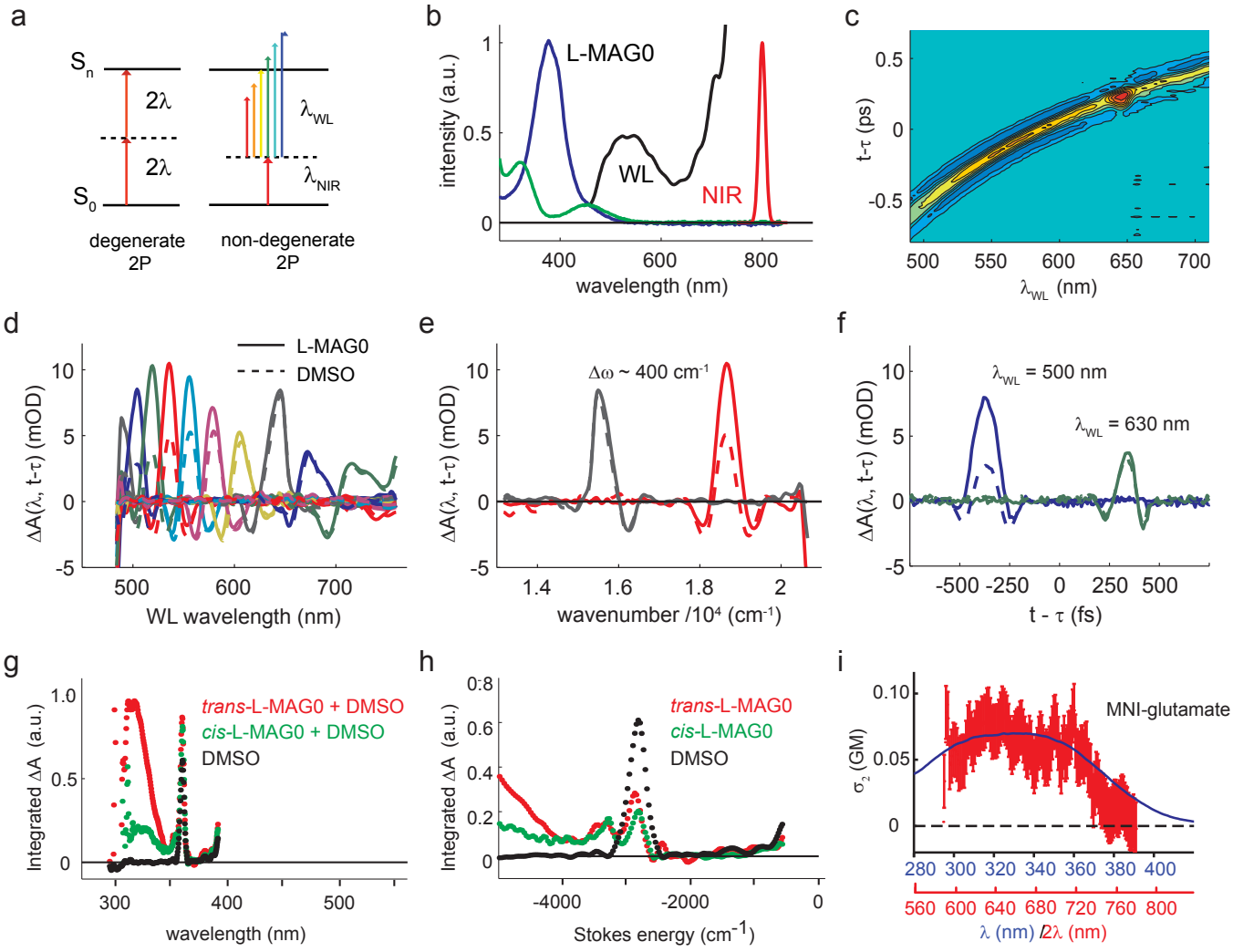

Carroll_Figure S4

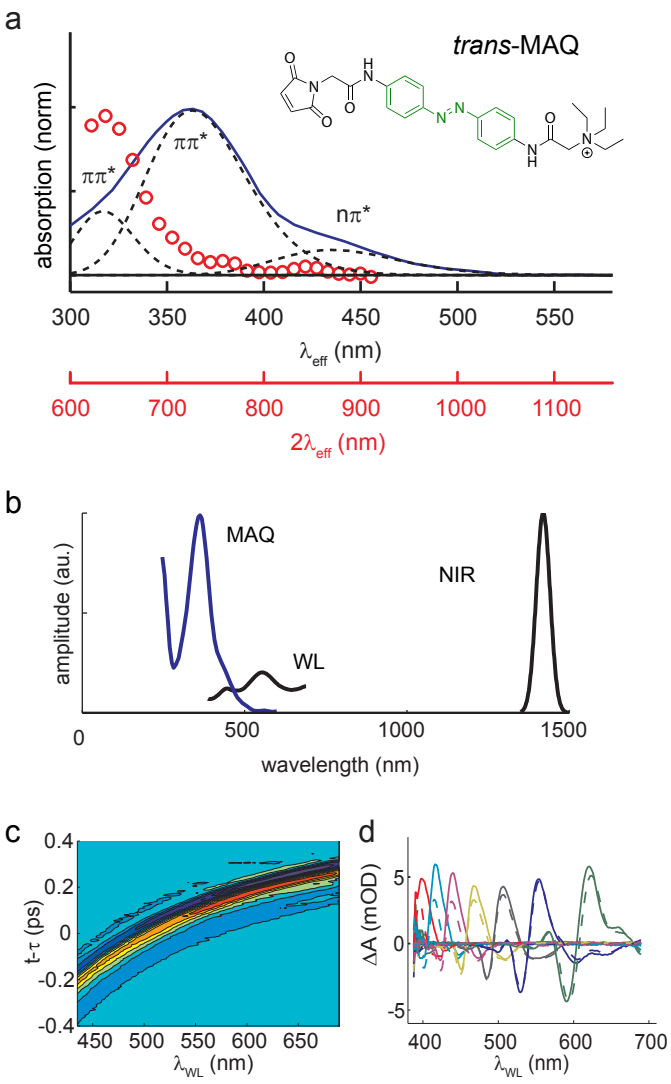

Carroll_Figure S5

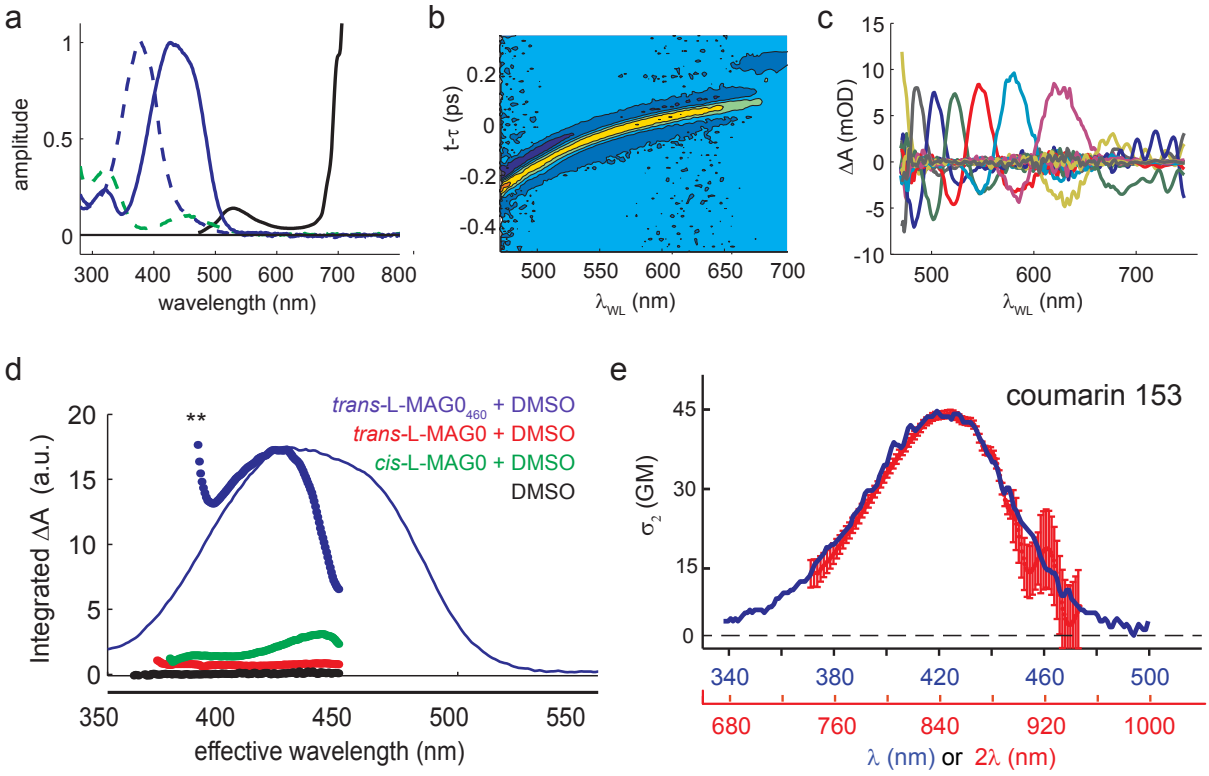

Carroll_Figure S6

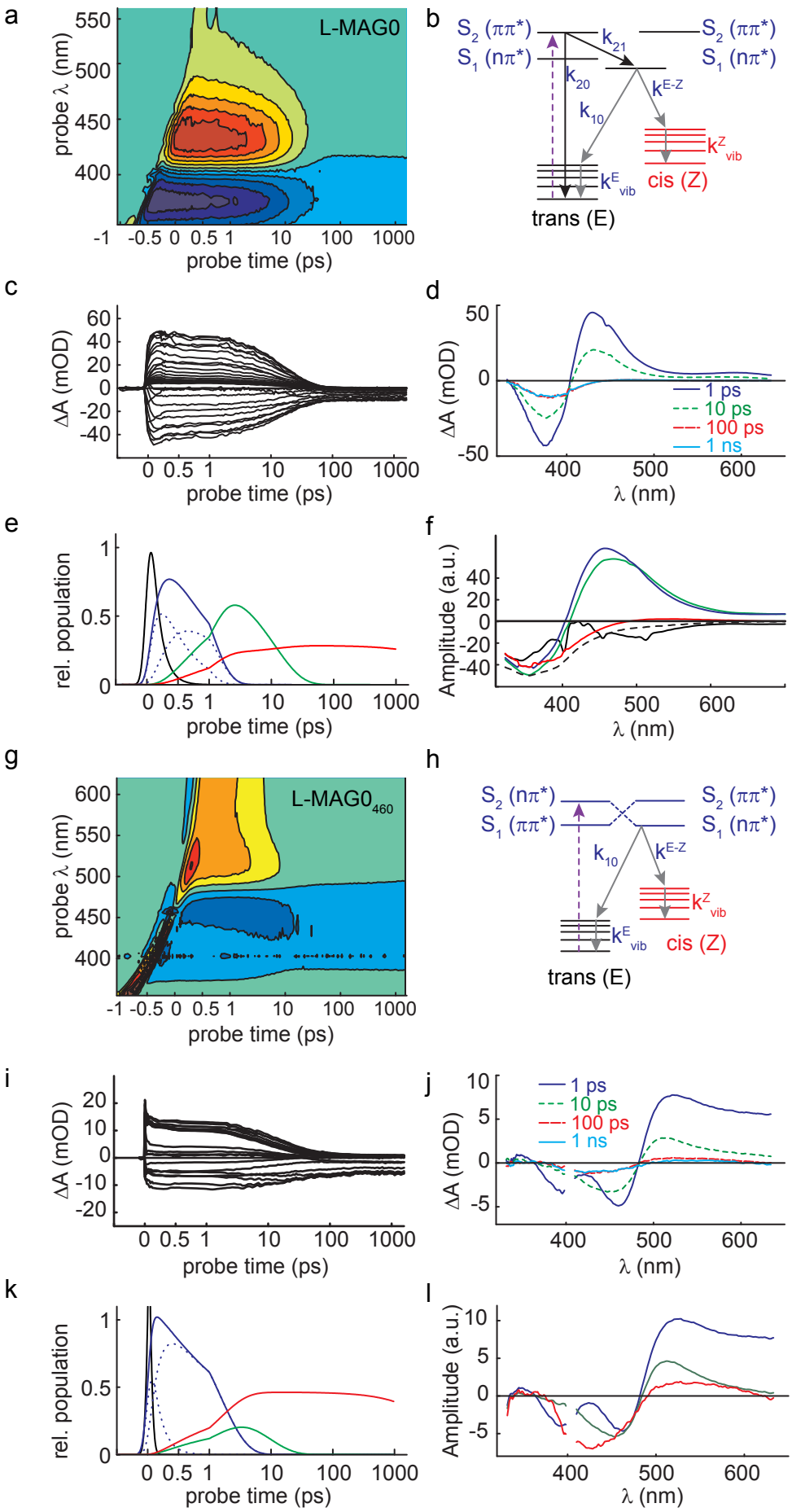

Carroll_Figure S7

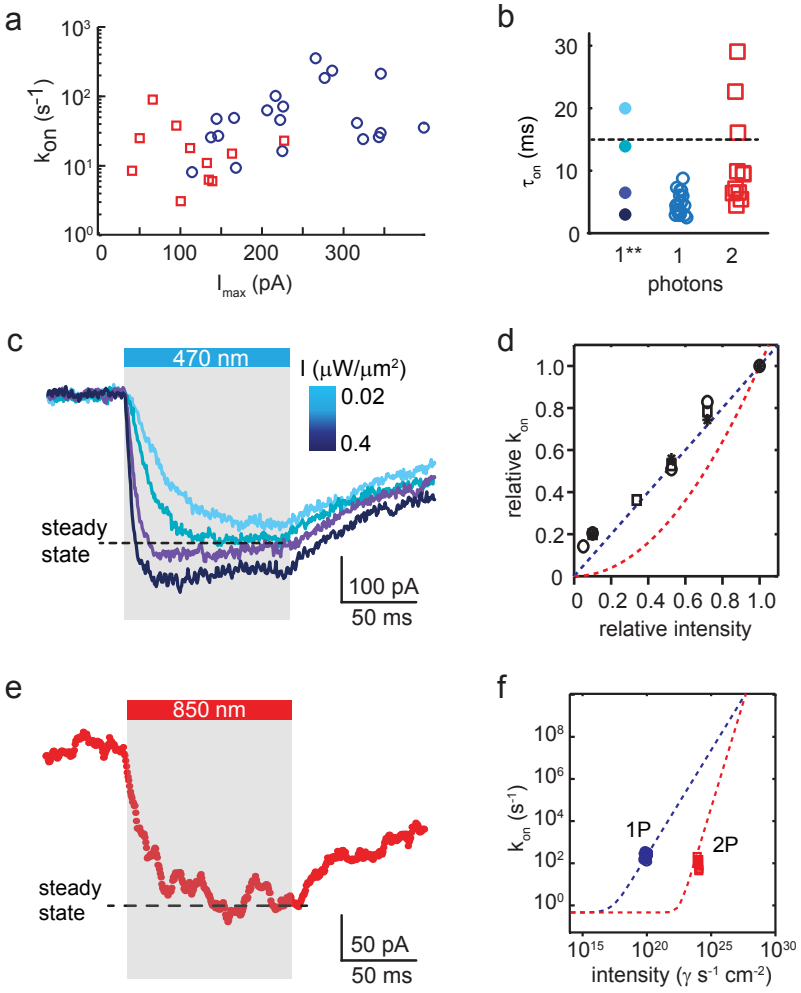

Carroll_Figure S8